Evolution of the free energy of the GaN(0001) surface based on first-principles phonon calculations

Pawel Kempisty [1,2,*] and Yoshihiro Kangawa [2,3]

[1] Institute of High Pressure Physics, Polish Academy of Sciences, Sokolowska 29/37, 01-142 Warsaw, Poland
[2] Research Institute for Applied Mechanics, Kyushu University, Fukuoka 816-8580, Japan
[3] Center for Integrated Research of Future Electronics, Institute of Materials and Systems for Sustainability, Nagoya University, Nagoya 464-8603, Japan

(Received 21 December 2018; revised manuscript received 31 July 2019; published 16 August 2019)

In this paper, we present systematic improvements to a method that allows us to determine the surface phase diagrams based on *ab initio* calculations and atomistic thermodynamics. In particular, we include a contribution derived from thermal vibrations of the surface, which is usually omitted in such analysis. On the basis of first-principles phonon calculations, we determine a zero-point vibrational energy and thermal dependencies of vibrational entropy and free energy for atoms and molecules adsorbed on the surface. A series of polar GaN(0001) surfaces are examined. Significant changes are observed in the surface phase diagrams compared to the diagrams obtained by standard density-functional theory calculations without phononic contributions.

DOI: 10.1103/PhysRevB.100.085304

I. INTRODUCTION

Gallium nitride (GaN) is one of the most promising materials that is applied in next-generation high-power electronic devices because of its excellent high-voltage and high-current capacity combined with high thermal conductivity. GaN power transistors can realize high-speed switching along with the simultaneous increase in the miniaturization of electronic devices. Recent studies have mainly focused on the development of vertical GaN power devices for use in electric vehicles [1–3]. For further development of these devices, it is necessary to obtain high-purity materials and methods to introduce intentional dopants. In epitaxial methods, dopants and impurities are incorporated at various concentrations depending on the direction of growth of the crystals. Unfortunately, some information about phenomena occurring at the surface of the crystal is not straightforwardly accessible in typical growth experiments. Therefore, theoretical studies on the surface properties and point defects in the subsurface layers are still needed to improve our knowledge and also the quantitative model. A recent study has shown that the change in surface reconstruction significantly affects the subsurface barriers, thereby limiting the incorporation of carbon into the layers of GaN [4]. Thus, understanding the surface thermodynamics is very important from the experimental point of view.

The conventional thermodynamic analysis for growth of crystals by vapor phase epitaxy assumes a gas-solid equilibrium. In 2001, Kangawa *et al.* developed an *ab initio*-based approach in which the free energy of the vapor phase was included [5]. The primary idea of this method is based on a comparison of the values of the chemical potential of gas $\mu^{\rm gas}$ with adsorption energy $E_{\rm ad}$ determined by density-functional theory (DFT) calculations to consider the adsorption/desorption behavior of adatoms or molecules. Within this approximation, thermal dependencies were considered only for the gas phase because the DFT method describes the system at temperature $T = 0\,{\rm K}$. This concept was efficiently used for polar, nonpolar, and semipolar nitride surfaces [6–10]. Some of the most popular articles on GaN(0001) surface phase diagrams were published by Van de Walle and Neugebauer [11,12]. They determined the most stable surface structures by comparing their formation energy ΔE^f. This parameter was defined as the energy difference between the reconstructed and the reference (clean) surface using the following formula:

$$\Delta E^f = E^{\rm DFT}_{\rm rec} - \left(E^{\rm DFT}_{\rm ref} + \sum_i n_i\mu_i\right) = \Delta E^{\rm DFT} - \sum_i n_i\mu_i \quad (1)$$

where n_i is the number of atoms with specified chemical potentials μ_i added to the reference clean surface from the reservoir. The $\Delta E^{\rm DFT}$ symbol denotes a simple difference in the total energy of two systems representing surfaces and determined by DFT calculations. It is clearly evident that in this formula there are no terms related to the entropy, neither configurational nor vibrational, of the surface. Justification of this is based on two statements. First, solid phase entropy is much lower compared to entropy of gas phase. Second, entropies of different surface terminations of the same solid are of similar order of magnitude and are comparable to entropy of bulk. The last assumption can be applied especially in case of clean surfaces and errors in such approach should be very small. However, it is known that the energy of an atom shifted from the bulk to the surface changes a little due to a different number of existing bonds. From the point of view of computational analysis, this surface energy can be relatively easily determined using a slab model with two identical symmetrical surfaces. In the case of polar GaN surfaces, such a procedure is not possible directly because there are two different surfaces: Ga-terminated and N-terminated. One needs to build an auxiliary system, for example, wedge-shaped geometry, that helps to determine the energy of at least one of the

*Corresponding author: pkempisty@unipress.waw.pl

 ©2019 American Physical Society

surfaces [13]. Therefore, a different approach is often used in which the reference system is not bulk but a selected surface, usually a clean surface, as given in Eq. (1). Recently, Kusaba *et al.* proposed an improved method which incorporates surface energies obtained by DFT calculations [14]. They set the bulk as a reference system and included an extra term $\Delta E_{\text{surface-bulk}}$ to calculate the Gibbs energy of the surfaces. It is noteworthy and extremely important that the location and environment of surface atoms are also associated with a change of vibrational entropy in relation to that in the bulk. The local change of the strength of atomic bonds at the surface causes shifting of the frequency of the atomic vibration. That is, reconstructed surface structure influences the vibrational entropy of the system. Particles on the surface can also diffuse more easily than in the bulk, allowing for more frequent configurational changes. In turn, considering the transition of the particle from a gaseous state to an adsorbed state on the surface, most of the translational and rotational entropy of the particle would be lost due to the reduction of degree of freedom. Various scenarios should be considered for the vibrational part, depending on whether the adsorbate is an atom or a molecule. In case of a monatomic molecule, translational entropy would be lost (not whole, because the adatom can move on the surface), but its thermal oscillations in the crystal lattice contribute to vibrational entropy. A molecule that has adsorbed in an unchanged molecular form largely retains the spectrum of internal vibrations, while during dissociative adsorption this spectrum is transformed. In the case of surfaces with a very complex adsorbate consisting of foreign atoms, vibrational entropy of the adsorbate can reach a significant value because the frequencies of vibrations can be completely different than in the crystals.

Unfortunately, changes of the free energy related to thermal vibrations were very often omitted, which could cause serious errors in the quantitative description. There were only a few studies where the vibrations were also considered. For example, Grabow *et al.* studied the removal of oxygen from the GaN surface by annealing in ammonia atmosphere and Lymperakis *et al.* studied hydrogen adsorption on a nonpolar GaN(1-100) surface [15,16]. Recently, we included vibrational properties to analyze the adsorption of H on GaN(0001) and AlN(0001) surfaces [17,18]. The primary reason why phononic calculations were often skipped is their time-consuming nature. Therefore, they were chiefly used in small bulk systems. Current development of computing power enables also including this factor for surface analysis. In this paper, we aimed to introduce this phononic factor and show how it improves the accuracy of theoretical models. First-principles phonon calculations allow us to determine various thermal properties for the solid phase and to model the hot surfaces existing during growth processes. We are particularly interested in epitaxial growth methods such as metal organic vapor phase epitaxy (MOVPE) and hydride vapor phase epitaxy (HVPE).

II. CALCULATION METHODS

A. Total energies and structures

The aforementioned studies used SIESTA software and associated tools for the calculations [19–21]. Energies of systems and force constant matrices were determined within the framework of DFT by using general gradient approximation to the exchange-correlation (XC) functional. We used a version of Perdew-Burke-Ernzerholf potential with parameters β, μ, and κ fixed by the jellium surface (Js), jellium response (Jr), and Lieb-Oxford bound criteria, respectively [22,23]. SIESTA uses numerical atomic orbitals as a basis set and norm-conserving pseudopotentials. Cutoff radii of the pseudopotentials and the size and range of the basis were optimized to obtain a good accuracy of thermochemical parameters such as the enthalpy of formation. The following size of the basis was used: N—quadruple zeta plus polarization, H and pseudo-H—quintuple zeta plus double polarization, Ga—triple zeta for s, p channel and double zeta for $3d$ electrons. A real-space grid was generated using an equivalent plane wave cutoff equal to 360 Ry. The following lattice constants were obtained for bulk GaN: $a = b = 3.208$ Å and $c = 5.222$ Å with the u parameter equal to 0.3767. They are compatible with $a = b = 3.189$ Å and $c = 5.185$ Å measured by x-ray diffraction by Leszczynski *et al.* [24].

In the first step, the surface structure was relaxed based on a 2×2 slab model with the thickness of eight GaN layers. The geometries of the considered reconstructed GaN(0001) surfaces are shown in Fig. 1. The pseudohydrogen atoms with an atomic number of 0.75 were used to saturate the dangling bonds of nitrogen at the bottom of the slab [26]. To compensate the artificial electric field in the vacuum created by the dipole moment of the system, a slab dipole correction was used [27]. For these systems, the Brillouin zone was sampled with a $5 \times 5 \times 1$ Monkhorst-Pack k-point mesh. During a geometric optimization, all atoms in the slab were relaxed until the atomic forces descended below 0.0001 eV/Å.

B. Lattice dynamics

To investigate the thermal properties, phononic calculations were performed using a direct method in harmonic approximation. The ground state of the vibration can be approximated reasonably well by a harmonic potential. This means that the phonon frequencies are treated as volume independent, and the thermal expansion coefficient is zero at all temperatures. Deviations from the harmonic expression are only really significant at high temperatures and also in phonon transport theories. Anharmonicity mainly affects the thermal conductivity, but we do not investigate this property here so we can apply the standard harmonic model. Introducing a quasiharmonic or an anharmonic approximation would improve the description even more, but at this stage this is not necessary. For the phononic calculations, larger supercells were built by multiplying the previous structures by a factor of 3×3, resulting in systems consisting of 610–730 atoms. These large systems were used to calculate the force constantmatrices by finite displacement method. Only Γ-point sampling was used in this step of the calculations. A displacement of 0.02 Bohr (0.011 Å) in each direction ($-x$, $+x$, $-y$, $+y$, $-z$, $+z$) was applied for every atom in a centrally located cell. In the harmonic approximation, the obtained force constant matrix is transformed into the dynamical matrix D, and the frequency of the vibrations of atoms is determined by solving an eigenvalue problem of matrix D.

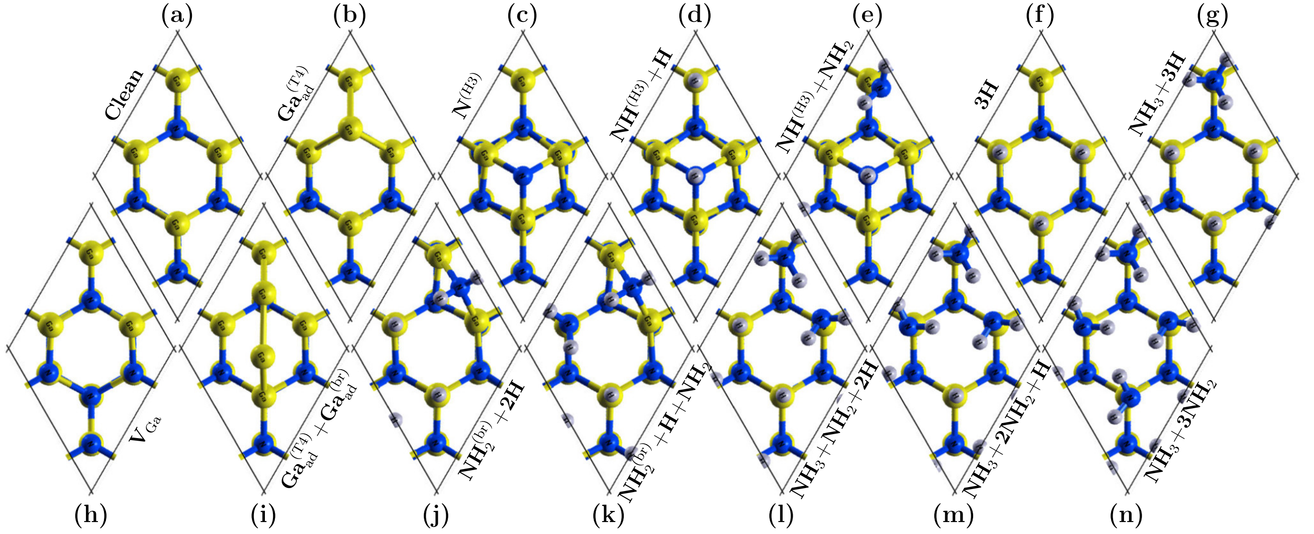

FIG. 1. Geometric configurations of selected reconstructed GaN(0001) surfaces. The graphics were generated by the XCRYSDEN package [25].

More information on the phonon calculation technique can be found elsewhere [28–30].

Based on the vibrational spectra, several properties, such as the zero-point vibrational energy E^{ZP}, vibrational energy E^{vib}, constant volume heat capacity C^{vib}, entropy S^{vib}, and free energy F^{vib} can be determined as functions of temperature T:

$$E^{\mathrm{ZP}} = \sum_j \frac{\hbar\omega_j}{2}, \tag{2}$$

$$E^{\mathrm{vib}}(T) = k_B T \sum_j \frac{x_j}{\exp(x_j) - 1},$$

$$\text{where} \quad x_j = \frac{\hbar\omega_j}{k_B T}, \tag{3}$$

$$C^{\mathrm{vib}}(T) = k_B \sum_j \frac{x_j^2 \exp(x_j)}{[\exp(x_j) - 1]^2}, \tag{4}$$

$$S^{\mathrm{vib}}(T) = k_B \sum_j \left\{ \frac{x_j}{\exp(x_j) - 1} - \ln[1 - \exp(-x_j)] \right\}, \tag{5}$$

$$F^{\mathrm{vib}}(T) = k_B T \sum_j \ln[1 - \exp(-x_j)], \tag{6}$$

where $\hbar$, k_B, and ω_j are the reduced Planck constant, the Boltzmann constant, and the angular frequency of each jth mode of vibration, respectively. Equations (2)–(6) have a universal form but, in the case of crystals, the dependence on the wave vector should be included, that is, $\omega_j \to \omega_j(\vec{k})$. Therefore, it is necessary to perform integrals over the first Brillouin zone or summation over special k-points [31,32]. In the present study, the sampling of k-space was done on a $45 \times 45 \times 3$ grid equivalent to 6075 points.

C. Free energy of solids and surfaces

Assuming that our considerations are limited to nonextreme pressure, we can neglect the impact of pressure on the solid and focus only on temperature dependencies. Our task is to shift from the absolute zero temperature to any given temperature T. We can define the Gibbs free energy of a slab via enthalpy H and entropy S:

$$G^{\mathrm{slab}}(T) = H(T) - TS(T),$$

$$\text{where} \quad H(T) = E^{\mathrm{DFT}} + E^{\mathrm{ZP}} + \int_0^T C^{\mathrm{vib}}(T)dT \tag{7}$$

$$\text{and} \quad S(T) = S^{\mathrm{vib}}(T) + S^{\mathrm{conf}},$$

whereby C^{vib} should formally be the heat capacity at constant pressure C_p, but in the case of the solid, one can approximate it by the constant volume heat capacity C_V from Eq. (4). At low-temperature range, these two parameters are almost identical. The discrepancy appears at high temperatures, but we can treat it as a systematic error that will disappear if we work on the differences in parameters between the systems. The S^{conf} term is the configurational entropy of the surface which is related to the position of its constituent particles. We can treat each surface in Fig. 1 as a separate macrostate where a series of microstates with the same energy is implemented by changing the arrangement of particles in the surface nodes. According to the statistical definition of the Boltzmann entropy, S^{conf} is defined as the logarithm of the number of possible independent configurations W that can realize a given system:

$$S^{\mathrm{conf}} = k_B \ln W. \tag{8}$$

The number of available microstates for N surface sites filled with n particles of i species can be counted using an ideal mixing rule:

$$W = \frac{N!}{\prod_i n_i!}, \quad \text{where} \quad \sum_i n_i = N. \tag{9}$$

For a large number of particles, the Stirling approximation $\ln N! \approx N \ln N - N$ can be applied, which leads to a simple formula:

$$S^{\mathrm{conf}} = -k_B \sum_i x_i \ln x_i, \tag{10}$$

where $x_i = n_i/N$ denotes the fraction of ith surface sites. Depending on the case, there are several coverage coefficients x_i related to different species in the adsorbate, i.e., x_N, x_{Ga}, x_H, x_{NH}, x_{NH_2}, and x_{NH_3}. It is obvious that the more components are mixed, the higher is the entropy.

We can convert Eq. (1) taking into account the full form of Gibbs energy for the system representing the surface in contact with the gas phase. Please keep in mind that the influence of pressure on the solid and its surface (the $p\Delta V$ term) is treated here as negligibly small [17]. Then, the Gibbs free energy difference ΔG^f for surface formation can be written as follows:

$$\Delta G^f(p,T) = \Delta E^{\rm DFT} - \sum_i n_i\mu_i(p_i,T) + \Delta E^{\rm ZP} + \int_0^T \Delta C^{\rm vib}(T)dT - T\Delta S^{\rm vib}(T) - T\Delta S^{\rm conf}, \tag{11}$$

where Δ means the difference between the reconstructed and the reference surface. Next, we can transform Eq. (11) into a more concise form introducing Helmholtz free energy $\Delta F = \Delta E - T\Delta S$:

$$\Delta G^f(p,T) = \Delta E^{DFT} - \sum_i n_i\mu_i(p_i,T) + \Delta E^{\rm ZP} + \Delta F^{\rm vib}(T) - T\Delta S^{\rm conf}. \tag{12}$$

D. Chemical potential of gas phase

Formerly, the thermodynamic formalism, Eq. (1), was commonly used to determine the equilibrium state of the surface as a function of composition [34]. In the case of GaN epitaxy, μ_{Ga} varies over the thermodynamically allowed range: $\mu_{\rm Ga[bulk]} + \Delta H^f[{\rm GaN}] < \mu_{Ga} < \mu_{\rm Ga[bulk]}$, the upper limit corresponds to Ga-rich conditions, the lower limit to N-rich ones ($\mu_N = \mu_{\rm N[N_2]}$) [11]. The GaN formation enthalpy, $\Delta H^f[{\rm GaN}]$, has been estimated to be -1.17 eV [35]. Therefore, the allowable range of $\Delta\mu_{Ga} = \mu_{Ga} - \mu_{\rm Ga[bulk]}$ can be expressed as $-1.17\,{\rm eV} < \Delta\mu_{Ga} < 0\,{\rm eV}$. In the actual experiments, however, it is difficult for an operator to link the value of $\Delta\mu_{Ga}$ with experimental parameters, i.e., input partial pressure of a particle i, p_i, and growth temperature, T. To compare experimental results with theoretical ones, it is necessary to clarify the correlation between μ_i and epitaxial growth parameters (p_i, T). Moreover, from the theoretical point of view, μ_i should be given as a function of p_i and T because the vapor phase and the surface are close enough to thermal equilibrium under typical MOCVD and HVPE conditions. By considering gaseous reservoirs in the growth system, we can link μ_i with p_i and T. In the following paragraph, we briefly present two basic ways to link the value of μ_i with the gas phase at a given pressure p_i and temperature T.

We would like to comment on the parameters relating to the vapor phase, which can be treated as a reservoir of particles in Eqs. (1), (11), and (12). The chemical potential μ_i, partial molar Gibbs free energy of the ith species, is defined as a sum of DFT total energy of an isolated particle, its zero-point vibrational energy, and the term dependent on the pressure and temperature of the gas phase:

$$\mu_i(p_i,T) = E_i^{\rm DFT} + E_i^{\rm ZP} + \mu_i^{\rm gas}(p_i,T). \tag{13}$$

The ideal gas approximation (there are no interactions among the atoms or molecules) can be applied to determine the properties of gas. Usually, the range of application of this approach should not exceed the pressure of several kilobars [10].

The formula derived from statistical mechanics, based on the partition functions ζ of an ideal gas including translational, rotational, and vibrational motions as well as the degree of degeneracy of the electron's energy level g, is useful for calculating the value of chemical potential [33]:

$$\mu^{\rm gas}(p,T) = -k_BT\ln(g\,\zeta_{\rm tran}\zeta_{\rm rot}\zeta_{\rm vib}\,k_BT/p). \tag{14}$$

The classical expression for the partition functions are the following:

$$\zeta_{\rm tran} = \left(\frac{2\pi mk_BT}{h^2}\right)^{3/2}, \tag{15}$$

$$\zeta_{\rm rot} = \frac{\sqrt{\pi I_AI_BI_C}}{\sigma_{\rm rot}}\left(\frac{8\pi^2k_BT}{h^2}\right)^{3/2}, \tag{16}$$

$$\zeta_{\rm vib} = \prod \frac{1}{1-\exp(-h\nu_j/k_BT)}, \tag{17}$$

where m is the mass of a particle; h is the Planck's constant; I_A, I_B, and I_C are the principal moments of inertia; $\sigma_{\rm rot}$ is the rotational symmetry number; and ν_j is the frequency of jth vibrational mode.

The second way is to use the data from standard thermochemical tables; for example, the NIST Chemistry WebBook database [36]. It should be noted that the properties are usually specified there in relation to standard conditions of temperature $T^\circ = 298.15$ K and pressure $p^\circ = 1$ bar. Therefore, we have to consider the transition between these conditions and the reference state of zero that exists in the DFT calculations. Then, the expression for the chemical potential of gas phase at given T and p takes the following form:

$$\mu^{\rm gas}(p,T) = [H^\circ - H^0] + \int_{T^\circ}^T C_p(T,p^\circ)dT - TS(T,p^\circ) + k_BT\ln\frac{p}{p^\circ}, \tag{18}$$

where $H^\circ = H(T^\circ, p^\circ)$ is the standard enthalpy, the $[H^\circ - H^0]$ term defines the change of standard enthalpy between 298.15 K and 0 K, both the constant pressure heat capacity C_p and the entropy S are specified at pressure p° = 1 bar. More details about the origin of Eq. (18) can be found, for example, in the paper by Jackson and Walsh [37].

III. RESULTS AND DISCUSSION

A. Bulk properties

First, we would like to present the obtained phonon band structure and phonon density of states for bulk GaN [see Fig. 2(a)]. Our results look essentially the same as those calculated by other authors and close to experimental [39–41]. The comparison of some calculated Γ-point phonon frequencies versus the experimental frequencies measured by Raman

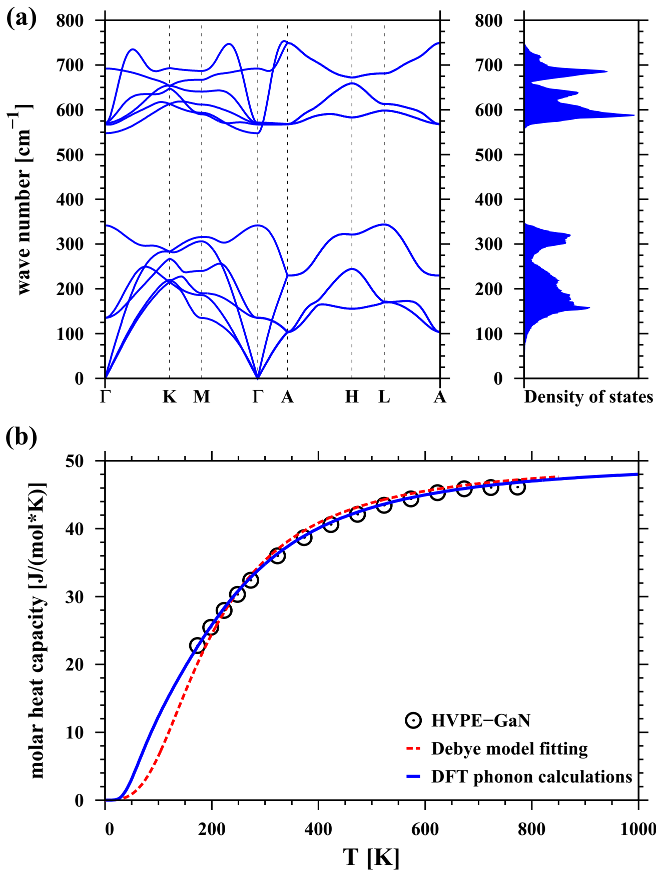

FIG. 2. (a) Phonon dispersion relation and phonon density of states calculated for bulk GaN. (b) Molar heat capacity at a constant volume for GaN; black open circles—data from the measurements on hydride vapor phase epitaxy (HVPE) GaN samples by Bockowski *et al.* [38]; red curve—Debye model fitting with $T_D = 817$ K; blue curve—present DFT phonon calculations.

spectroscopy is presented in Table I [40]. In the case of longitudinal A1(LO) and E1(LO) modes, there are large discrepancies between DFT-predicted and experimental values. This is a very known inconsistency of the direct method for polar materials, discussed in the literature [29,42]. Because it is a systematic error present in every considered system, the relative differences of values between the systems will be less prone to this error. Next, we show that, based on these dependencies, we can correctly determine the material properties. For this purpose, we show in Fig. 2(b) the molar specific heat at constant volume of GaN. Our theoretical curve is in good agreement with the measurements of HVPE-GaN samples by the hyperflash method published by Bockowski *et al.* [38]. Since the measurements were performed under constant pressure conditions, it is also proof that in the range of lower and medium temperatures there is no significant difference between the heat capacity C_p and C_V.

TABLE I. Calculated and experimental frequencies (in cm^{-1}) of some phonons in GaN at the center of the Brillouin zone.

Mode type	DFT calculations	Raman [40]
E_1(LO)	571.3	746.6
A_1(LO)	567.4	739.3
B_1	692.1	
E_2	570.6	569.2
E_1(TO)	567.0	560.0
A_1(TO)	547.6	533.5
B_1	341.7	
E_2	134.9	144.2

B. Thermodynamic properties of surfaces

The primary results are focused on the calculation of thermal properties of a number of GaN(0001) surfaces with various reconstructions and adsorbates. Figure 1 shows the geometry of systems considered by us. We limited our analysis to surfaces with a 2 × 2 periodicity as one of the most often reported [43]. In general, for a more detailed discussion a larger periodicity should be also considered, for example 4 × 4, 5 × 5, 6 × 4, or $\sqrt{3} \times \sqrt{3}$ which were observed in some experiments [43]. A clean surface with a 2 × 1 reconstruction was taken as a reference system due to its lower energy, as reported previously [44]. In the case of a flat 1 × 1 surface, we observed the existence of a soft mode (negative frequencies) in the phonon's band structure, which confirms the instability of this structure.

Molecules and atoms adsorbed on the surface introduce additional vibrational modes to the phonon spectra. These modes are often very different in frequency from the vibrations of atoms in the volume material, as shown in Fig. 3. The spectra in the top panel contain high-frequency modes from vibrations of H adatoms, NH_3 admolecules, and amino radicals attached to the GaN(0001) surface. The presence of nondispersive modes confirms that some adsorbed molecules and radicals retain their molecular nature. The frequencies of these vibrations are consistent with previously reported data [15]. Simultaneously, the vibrational modes of atoms that are bonded with the adsorbate are also shifted because of the local change in the bond strength between the atoms. Therefore, for surfaces with various adsorbates, different dependencies of the free energy as a function of temperature should be expected. In some temperature ranges, the corrections originating from the thermal vibrations of the system are fairly large, which should be included in the thermodynamic calculations. In the case of a low temperature range, the crucial factor is the zero-point vibrational energy, whereas in the case of high temperature range the entropy contribution is dominant. In a certain intermediate temperature, both these terms can delete each other, so even standard DFT calculations without phononic contribution can give the correct result.

In this paper, we calculated changes in the zero-point vibrational energy and in the vibrational free energy for a few selected surfaces presented previously in Fig. 1. Figures 4(a) and 4(b) show some examples of behavior of ΔF^{vib} in relation to the temperature, and it is easy to see different slopes of curves related to the different surfaces. For the surfaces with complex adsorbates, the energy differences originating from vibrations can reach significant values, which can be seen primarily for NH_3 and NH_2 admolecules. This type of

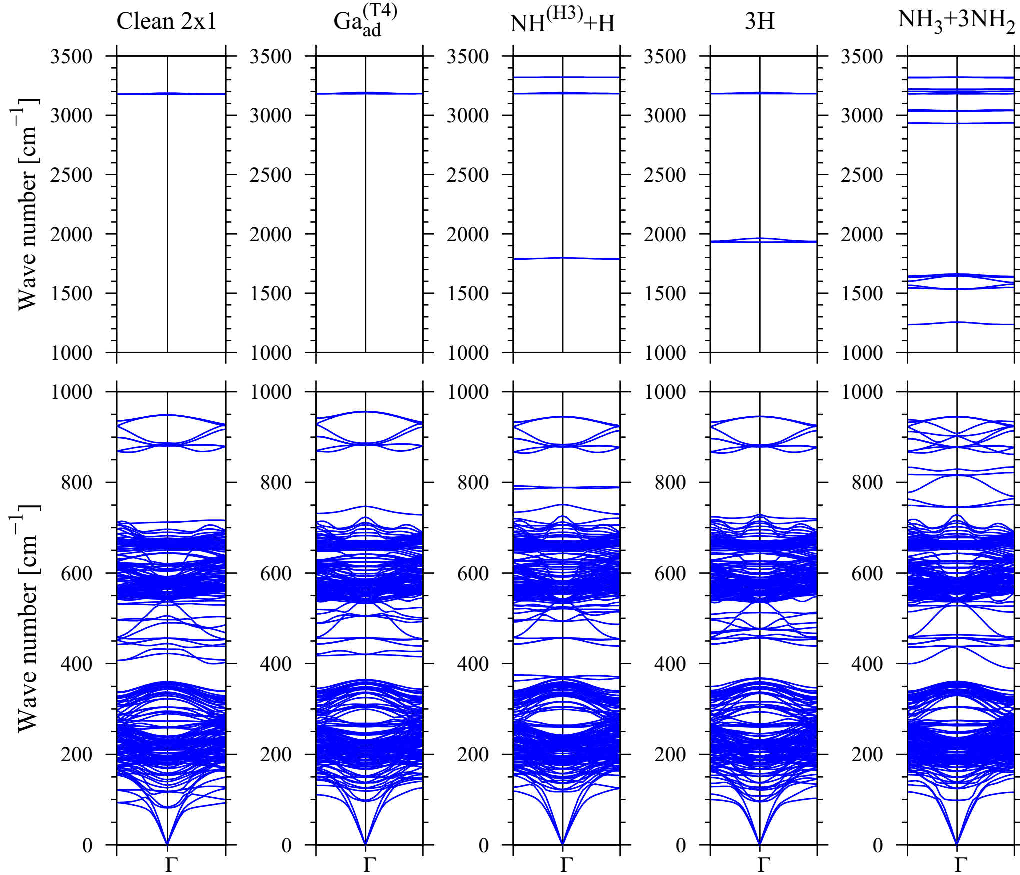

FIG. 3. Phonon dispersion relations for 2 × 2 slabs representing GaN(0001) surfaces with different adsorbate. Spectra in the top panel contain high-frequency modes from vibrations of H adatoms, NH_3 admolecules, and amino radicals, as well as the pseudo-H atoms of termination of the (000-1) side of the slab (approximately 3200 cm^{-1}). The bands in the range between 850 and 950 cm^{-1} are related to N atoms near slab termination.

adsorbed species mostly has typical high-frequency molecular vibrations; therefore, discrepancies in relation to the clean rigid surface increases. The vibrational part of the chemical potential of the molecule in the gas phase and of that adsorbed on the surface can be comparable.

According to Fig. 4(a), there is a relatively small thermal change of ΔF^{vib} between surfaces called $\mathrm{Ga}_{\mathrm{ad}}^{(\mathrm{T4})}$, $\mathrm{NH}^{(\mathrm{H3})} + \mathrm{H}$ and 3H [see Figs. 1(b), 1(d) and 1(f)]. However, there is also a component derived from zero-point vibrational energy, which brings an additional offset between these curves, as shown in Figs. 4(b) and 4(d). In most cases, the total correction due to ΔE^{ZP} and $\Delta F^{\mathrm{vib}}(T)$ gives a contribution which increases the Gibbs free energy of surfaces and therefore it acts as a destabilizing factor. The exceptions are the surfaces covered with Ga adatoms and also the $\mathrm{NH}^{(\mathrm{H3})} + \mathrm{NH}_2$ surface where the $\Delta E^{\mathrm{ZP}} + \Delta F^{vib}(T)$ term is negative in the high temperature range. It is worth noting the intersection of curves for $\mathrm{NH}^{(\mathrm{H3})} + \mathrm{H}$ and $\mathrm{NH}^{(\mathrm{H3})} + \mathrm{NH}_2$ surfaces may shift the relative point of mutual stability of these surfaces. For even higher temperatures (beyond the scale in Fig. 4), it seems that all curves will reach negative values. We do not present these data because they can be flawed due to the approximation of ground state of DFT and harmonic potential for phonons. Additionally, GaN becomes thermodynamically unstable at high temperature.

For the sake of convenience, we made a simple parametrization of the free-energy change as a function of temperature by fitting it to the following expression:

$$\Delta F^{\mathrm{vib}}(T) = a\, k_B T \ln\left[1 - \exp\left(-\frac{b}{k_B T}\right)\right], \tag{19}$$

where k_B is expressed in [eV/K] and the relevant fitting parameters a and b are presented in Table II. These data should be used as thermal corrections for the solid phase in models determining the stability of the GaN(0001) surface based on Eq. (12). This is only a relative change in comparison to the clean surface with a 2 × 1 reconstruction, attributable to an area equal to 2 × 2 surface cells. According to the results, at a temperature of 1300 K, typical for GaN growth by MOVPE or HVPE, surfaces with Ga adatoms gain an additional energy-lowering factor of approximately 0.24 eV for the case of single Ga and 0.82 eV for the Ga-Ga dimer. Such energies can be transformed into a change in gallium vapor pressure by one and over three orders of magnitude, respectively. This means that the partial pressure of gallium needed to cover the surface with Ga adatoms will actually be much lower than that estimated by the model without lattice vibrations.

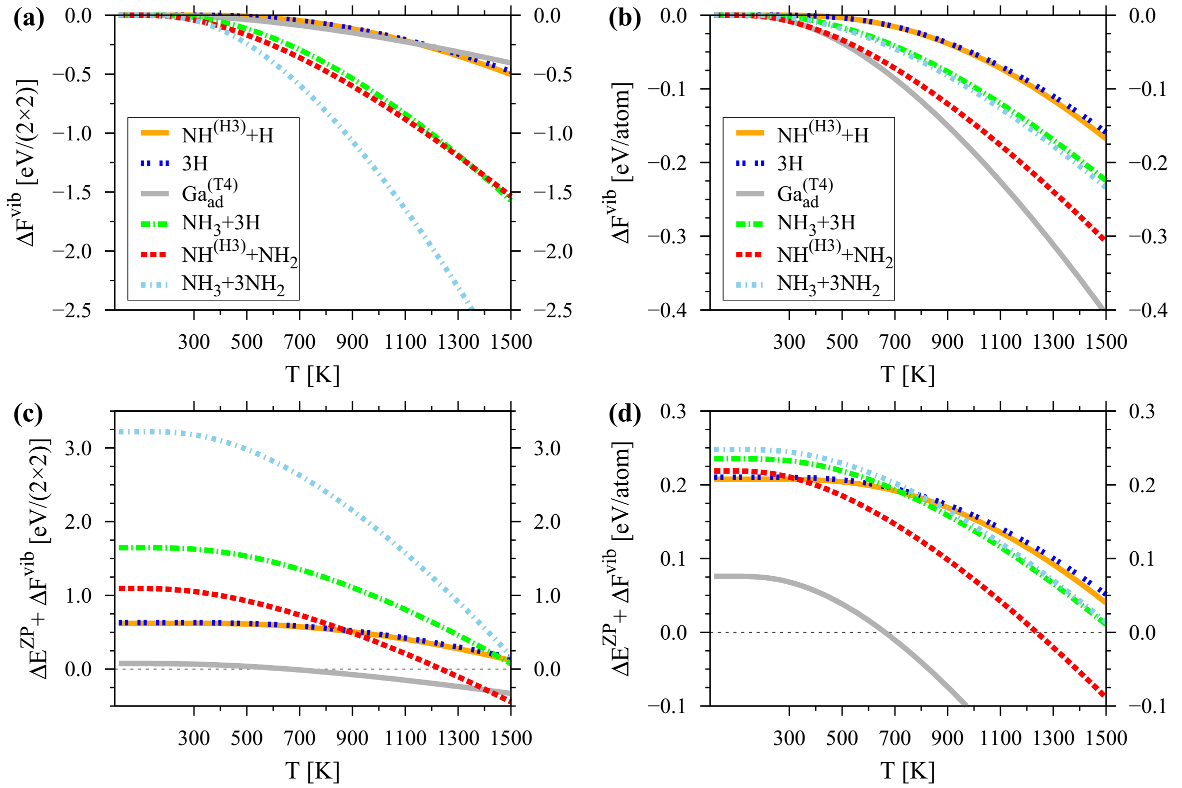

FIG. 4. Changes in the vibrational free energy versus temperature for the GaN(0001) surface covered with different adsorbates, determined in relation to clean surface with 2×1 reconstruction; (a), (b) $\Delta F^{\mathrm{vib}}(T)$ dependence; (c), (d) $\Delta F^{\mathrm{vib}}(T)$ dependence including zero-point ΔE^{ZP} offset. Graphs (a) and (c) show energies of the entire 2×2 surface cell, while graphs (b) and (d) show the average energy per atom.

C. Surface phase diagrams

Figure 5 shows the impact of the proposed thermal improvements on the surface phase diagrams for GaN(0001). These diagrams were prepared by selecting the lowest Gibbs free energies determined from Eq. (12). For simplicity, we applied the commonly used convention of plotting the diagram in the coordinates of the chemical potential of hydrogen μ_{H} and nitrogen μ_{N} (or gallium μ_{Ga}) proposed previously in Ref. [11]. This method assumes equilibrium conditions defined as follows:

$$\mu_{\mathrm{GaN}} = \mu_{\mathrm{Ga}} + \mu_{\mathrm{N}}. \tag{20}$$

Therefore, it is enough to use the potential of only one component, either N or Ga. This is a special case, because

TABLE II. Zero-point vibrational energy ΔE^{ZP} and parametrization of the changes of vibrational free energy ΔF^{vib} [parameters a and b in Eq. (19)] of selected reconstructed GaN(0001) surfaces. The reference system is a clean surface with a 2×1 reconstruction. The last column contains the sum of corrections $\Delta E^{\mathrm{ZP}} + \Delta F^{\mathrm{vib}}$ for temperature $T = 1300\,\mathrm{K}$ (close to typical GaN growth conditions in MOVPE or HVPE). Properties are expressed for 2×2 surface cells.

GaN(0001) surface	ΔE^{ZP}	Parameters of Eq. (19)		$\Delta E^{\mathrm{ZP}} + \Delta F^{vib}$
[2×2 cells]	[eV]	a [arb.u]	b [eV]	($T = 1300\,\mathrm{K}$) [eV]
$Ga_{ad}^{(T4)}$	0.076	3.275	6.257×10^{-2}	−0.235
$N^{(H3)}$	0.136	63.171	6.164×10^{-1}	0.107
$NH^{(H3)}+H$	0.623	12.157	1.673×10^{-1}	0.277
$NH^{(H3)}+NH_2$	1.094	10.553	5.060×10^{-2}	−0.103
3H	0.631	10.978	1.621×10^{-1}	0.301
NH_3+3H	1.647	15.689	7.981×10^{-2}	0.462
V_{Ga}	−0.002	−3.194	1.653×10^{-2}	0.709
$Ga_{ad}^{(T4)}+Ga_{ad}^{(br)}$	0.105	5.903	3.180×10^{-2}	−0.819
$NH_2^{(br)}+2H$	1.151	15.791	1.362×10^{-1}	0.529
$NH_2^{(br)}+H+NH_2$	1.632	16.268	7.908×10^{-2}	0.392
NH_3+NH_2+2H	2.149	20.826	8.445×10^{-2}	0.665
NH_3+2NH_2+H	2.682	24.334	7.619×10^{-2}	0.756
NH_3+3NH_2	3.221	28.355	7.406×10^{-2}	0.914

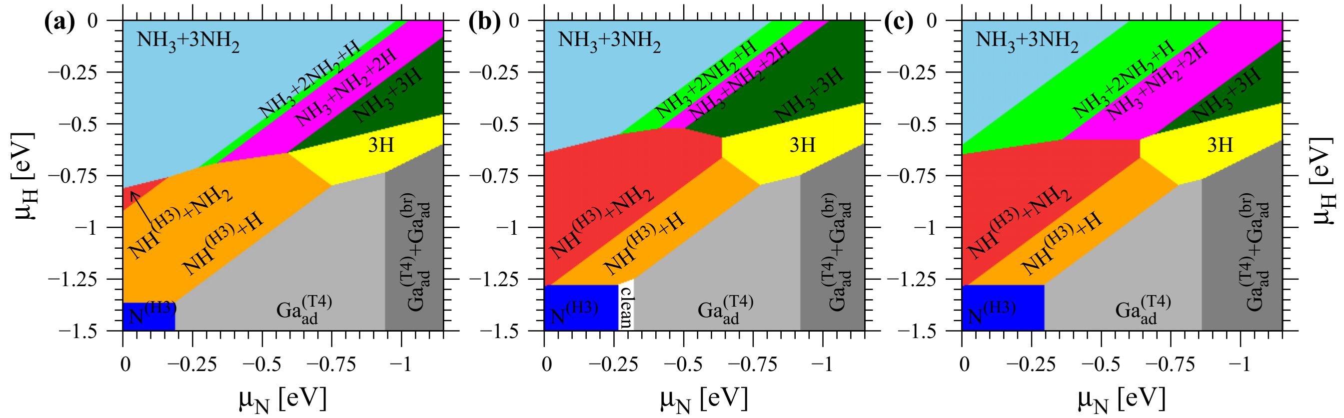

FIG. 5. Comparison of phase diagrams for the GaN(0001) surface obtained from DFT calculations: (a) Standard method based only on total energy, (b) including vibrational free energy at $T = 1300$ K, (c) including vibrational free energy at $T = 1300$ K, and configurational entropy. Diagrams were prepared assuming the global equilibrium conditions. Reference chemical potential levels are defined by conditions $T^\circ = 298.15$ K and $p^\circ = 1$ bar.

in general the value of μ_{GaN} can be lower than the sum of $\mu_{\mathrm{Ga}} + \mu_{\mathrm{N}}$, so a wider range of chemical potential of N (or Ga) should also be considered. The diagram in Fig. 5(a) was prepared in a standard way, so it is almost the same as those presented previously by other authors [7,11]. Small visual differences result from the use of different XC potentials, a larger number of considered surfaces, and due to shifting of the reference level of chemical potentials to standard state conditions ($T^\circ = 298.15$ K, $p^\circ = 1$ bar) instead of 0 K. Such a form of diagram was treated as universal, that is, the change of μ on both axes can be induced by temperature or/and pressure, but the color-coded map will always remain the same. The diagram in Fig. 5(b) includes the effects related to the thermal vibrations of the surface at $T = 1300$ K. Then, we should be aware that changes of μ_{N} and μ_{H} have to be considered as caused only by pressure or using other sources of considered species. This is a real physical situation when we conduct the epitaxial growth process at a constant temperature and we change the partial pressure of the reactants and/or the type of these reactants (another chemical compound of the same element). In this approach, a different diagram should be drawn for each temperature because the free energy of surface is a function of T. The primary difference between Figs. 5(b) and Fig. 5(a) is that the space of $\mathrm{NH}^{(\mathrm{H3})} + \mathrm{NH}_2$ surface is significantly enlarged at the expense of reducing the $\mathrm{NH}^{(\mathrm{H3})} + \mathrm{H}$ area. This is due to a larger contribution of the vibrational entropy of the NH_2 radical than that of the H adatom. The second important fact is the emergence of the clean surface region between the surface covered by N and Ga adatoms. Figure 5(c) shows an additional factor of surface configurational entropy. Therefore, the phase space of the adsorbate with a larger number of components is more extensive. A clean surface is virtually inaccessible because it has the lowest entropy.

In the actual experiments, an operator does not use μ_{N} and μ_{H} as crystal growth parameters. He sets the flow rates of gallium source gas, nitrogen source gas, and carrier gas, as well as the total chamber pressure, p, and substrate temperature, T, to control the ambient in the growth reactor. Therefore, it is useful for the experimentalists to know the relationship between the chemical potentials and crystal growth conditions, i.e., V/III ratio, p and T, to understand the meaning of the surface phase diagram. The information is useful to discuss the most probable surface reconstruction under the actual growth conditions. In the following paragraphs, we explain how to draw a typical MOCVD condition range in the μ_{N}–μ_{H} surface phase diagram (see Fig. 6 and related descriptions). Then, V/III–T surface phase diagrams are shown to discuss elementary growth processes under typical MOCVD experimental conditions (see Fig. 7 and related descriptions).

It is worth noting that there were some difficulties in accurately determining the value of chemical potential under growth conditions in epitaxial methods such as MOVPE or HVPE. In fact, the system is far from the equilibrium because there is forced flow of a mixture of injected gases. Fortunately, there is a steady state, so the quasiequilibrium approach can be applied. Various levels of the chemical potential might be considered for the same species. For example, μ_{N} and μ_{H} can

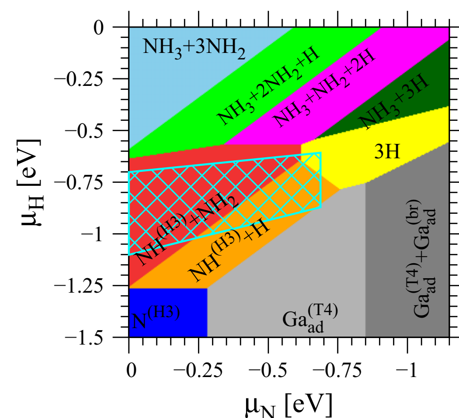

FIG. 6. Phase diagrams for the GaN(0001) surface at $T = 1253$ K. Shaded region corresponds to the expected range of the chemical potentials estimated for the typical MOVPE process at pressure $p = 150$ mbar and total flow of 8 slm with input molar fraction of ammonia 0.045, and H_2 or N_2 carrier gas.

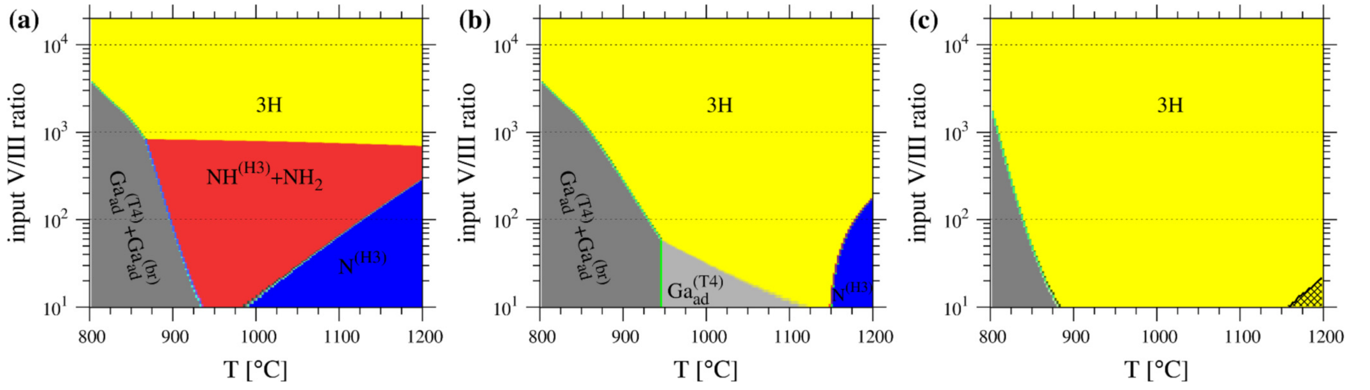

FIG. 7. Phase diagrams for the GaN(0001) surface obtained from DFT calculations for experimental set of low-pressure ($p = 26.7$ mbar) MOCVD process with (a) nitrogen carrier gas, (c) nitrogen with 2% of H_2 carrier gas, (b) hydrogen carrier gas.

be determined by the molecular form of N_2 and H_2 gases:

$$\mu_{\mathrm{N}} = 0.5\mu_{\mathrm{N}_2} \quad \text{and} \quad \mu_{\mathrm{H}} = 0.5\mu_{\mathrm{H}_2}. \tag{21}$$

as well as by the NH_3 vapor:

$$\begin{aligned}\mu_{\mathrm{N}} &= \mu_{\mathrm{NH}_3} - 1.5\mu_{\mathrm{H}_2},\\ \mu_{\mathrm{H}} &= (\mu_{\mathrm{NH}_3} - 0.5\mu_{\mathrm{N}_2})/3,\end{aligned} \tag{22}$$

In contrast to the equilibrium state, the chemical potential of individual components taken from Eqs. (21) and (22) are not equal. In particular, the values of μ for N ant H atoms originated from NH_3 molecules are higher than from N_2 and H_2 molecules. Therefore, ammonia is an effective source of N and H atoms settling on the surface. On the other hand, these atoms can fall away from the surface by forming their more stable molecular forms of nitrogen and hydrogen. Additionally, in the gas phase a partial decomposition of ammonia may also occur, so the effective available amount of this species will be reduced according to the formula

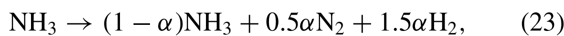

$$\mathrm{NH}_3 \rightarrow (1-\alpha)\mathrm{NH}_3 + 0.5\alpha\mathrm{N}_2 + 1.5\alpha\mathrm{H}_2, \tag{23}$$

where α is the decomposition factor that can vary over a wide range depending on temperature, pressure, type of carrier gas, reactor geometry, and flow rate. Similar dilemmas are in the case of the gallium source, where one can consider the dissociation of trimethylgallium or triethylgallium (TEG) and the existence of either atomic gallium or the form of various chemical compounds [45]. For all these reasons, the diagrams in Fig. 5 are not suitable for an accurate analysis of surface conditions during epitaxial growth. Nevertheless, these diagrams allow to estimate roughly the sequence of the surface arrangement and narrow the search area.

To illustrate the extent of the problem, we marked the thermodynamically accessible conditions for the MOVPE method in the phase diagram in Fig. 6. The parameters of a typical process were assumed, i.e., temperature 1253 K, total pressure 150 mbar, total flow of 8 slm (standard liter per minute) with input molar fraction of ammonia 0.045 and H_2 or N_2 carrier gas [46]. The shaded region shows the expected range of chemical potentials μ_{N} and μ_{H} estimated by taking their extreme values according to Eqs. (21) and (22). Only the higher level of μ_{N} corresponding to nitrogen originating from ammonia is considered. Moving from left to right side denotes the case when diluent gas is changed from nitrogen to hydrogen. Two different values of NH_3 decomposition factor $\alpha = 0.15$ for N_2 diluent and $\alpha = 0.05$ for H_2 diluent in Eq. (23) were assumed. The origin of these values will be discussed later. The top and bottom border correspond to the μ_{H} values obtained at the transition from the ammonia source to the molecular H_2 source, respectively. It is easy to see that the range of chemical potential change is very large and combining the diagrams with appropriate experimental conditions is very problematic. In our opinion, due to the multiplicity of parameters, it is conceptually difficult to create universal diagrams, but rather individual or more narrowed cases should be considered.

In the context of crystal growth, diagrams presented in Figs. 5 and 6 have a serious disadvantage. As mentioned, they were prepared assuming equilibrium conditions. Meanwhile, the growth process could take place if any supersaturation exists; in other words, if there is a deviation from the equilibrium state. The supersaturation can be expressed as a difference of input partial pressure p^{in} of the process limiting reactant and its equilibrium pressure p^{eq} obtained from the governing chemical reaction. In the case of the MOVPE process considered here, gallium is the limiting species and a simple chemical reaction that regulates growth of GaN is recommended [47–49]:

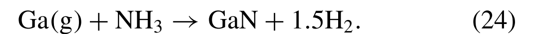

$$\mathrm{Ga(g)} + \mathrm{NH}_3 \rightarrow \mathrm{GaN} + 1.5\mathrm{H}_2. \tag{24}$$

The supersaturation can be defined as

$$\sigma_{\mathrm{Ga}}^{\mathrm{GaN}} = \frac{p_{\mathrm{Ga}}^{\mathrm{in}} - p_{\mathrm{Ga}}^{\mathrm{eq,GaN}}}{p_{\mathrm{Ga}}^{\mathrm{eq,GaN}}}. \tag{25}$$

On the other hand, one should be careful about the supersaturation associated with the equilibrium vapor pressure over liquid gallium:

$$\sigma_{\mathrm{Ga}}^{\mathrm{liq}} = \frac{p_{\mathrm{Ga}}^{\mathrm{in}} - p_{\mathrm{Ga}}^{\mathrm{eq,liq}}}{p_{\mathrm{Ga}}^{\mathrm{eq,liq}}}. \tag{26}$$

A positive supersaturation value in Eq. (26) means that condensation of liquid gallium may occur in the system. The values of metal vapor pressure $p^{\mathrm{eq,liq}}$ can be found in the

TABLE III. Atomic configurations of reconstructed surfaces and reference molecular configurations in the gas phase. It was assumed that each particle on the surface always comes from a source with a higher chemical potential and escapes to a state with lower chemical potential.

Surface	Gas
$Ga_{ad}^{(T4)}$	Ga
$N^{(H3)}$	$NH_3 - 1.5H_2$
$NH^{(H3)}+H$	$NH_3 - 0.5H_2$
$NH^{(H3)}+NH_2$	$2NH_3 - 1.5H_2$
3H	$NH_3 - 0.5N_2$
NH_3+3H	$2NH_3 - 0.5N_2$
V_{Ga}	−Ga
$Ga_{ad}^{(T4)}+Ga_{ad}^{(br)}$	2Ga
$NH_2^{(br)}+2H$	$2NH_3 - 0.5N_2 - H_2$
$NH_2^{(br)}+H+NH_2$	$2NH_3 - 0.5H_2$
NH_3+NH_2+2H	$3NH_3 - 0.5N_2 - H_2$
NH_3+2NH_2+H	$3NH_3 - 0.5H_2$
NH_3+3NH_2	$4NH_3 - 1.5H_2$

literature [50]. The issue of supersaturation is discussed in greater detail in the articles by the group of Z. Sitar [48,49,51]. Considering the above, the influence of gallium vapor pressure should be carefully analyzed and the chemical potential of this species should be explicitly calculated instead of using the generalized value of $\mu_{Ga} = \mu_{GaN} - \mu_N$ derived from the equilibrium condition defined by Eq. (20). In addition, the effective levels of chemical potentials of nitrogen and hydrogen should be also considered to express the incoming flux of active molecules with high values of μ, balanced by the escape of atoms to the state with lower μ. For each configuration of considered reconstructed surface, a reference state was defined with the assumption of a local gas–surface equilibrium. These systems are summarized in Table III. All aspects and parameters listed above were applied to determine the constraints of thermodynamically accessible conditions during epitaxial growth of GaN.

For the needs of the analysis, we adopted the experimental conditions described in Refs. [49,51]. They presented growth of GaN via metalorganic chemical vapor deposition (MOCVD) at temperature 1050 °C with varying V/III ratios and diluent gases. The total flow and pressure were set constant at 7.5 slm and 26.7 mbar, respectively. The V/III ratio was varied from 100 to 2000 by changing the NH_3 flow rate while the TEG flow rate of 280 sccm was kept constant. To obtain a very high V/III ratio, the ammonia flow was set constant at 5.9 slm and the TEG flow was changed accordingly. Based on this data and our first-principles calculations, we have created surface diagrams of GaN(0001) as a function of temperature and V/III ratio. These parameters are more convenient from the experimental point of view than the chemical potential. The nominal values of the input V/III ratio were changed by the ammonia decomposition factor α equal to 0.05 for H_2 diluent gas and 0.15 for N_2. Such values of α were adopted after analyzing the logarithmic derivative of ammonia supersaturation $(1+\sigma_{NH_3})$ as a function of the concentration ratio N_2/NH_3 and H_2/NH_3. The values beyond the inflection points were chosen so the changes in driving force were relatively smooth. In turn, the gallium supersaturation from Eqs. (25) and (26) was served for the control of GaN thermodynamic stability. The results are presented in Fig. 7. We considered three cases of carrier gas: pure nitrogen, nitrogen with the addition of 2% of H_2, and pure hydrogen [Figs. 7(a)–7(c), respectively]. When nitrogen is used, two regions related to the V/III ratio can be easily distinguished. For the low coefficient, going according to the temperature increase, the surface coverage varies from the gallium dimers, through the NH and NH_2 radicals, to N adatoms. For a high V/III ratio, 75% of the surface nodes are hydrogenated. If even a small amount of additional H_2 is added to the carrier gas, it causes large changes on the surface, as shown in Fig. 7(b). Hydrogen displaces amino radicals, and for the very low V/III ratio single Ga adatoms can appear. It is predicted that H adatoms (0.75 monolayer) will be dominant on the surface if a hydrogen carrier gas is used. Gallium coverage is also possible at lower temperatures and low V/III.

The presented diagrams and the transformation sequence of the surface coverage at a low V/III ratio fit well into the concepts of the existence of an additional surface barrier for incorporation of some dopants. We have reported the depth profiles of formation energy of carbon substituting nitrogen, C_N [4]. The results implied that there was a potential barrier for carbon incorporating from the growth surface into the crystal. The following statements were made basing on theoretical calculations: (i) change in the surface reconstruction causes the Fermi level pinning and accompanying surface band bending, (ii) change in the surface band bending varies the potential barrier for carbon incorporation, and (iii) change in the potential barrier influences the carbon concentration in the grown films. The proposed model has a universal character and can be adapted to other dopants, impurities, and materials. The discussions presented above indicate that a prediction of reconstructed structures on the growth surface is necessary to estimate impurity and/or dopant concentrations in the films. Controlling impurity and/or dopant concentrations is crucial to improve optical and electronic device properties. Figure 7 shows that the potential barrier may be related to the $NH^{H3} + NH_2$ reconstruction case of nitrogen carrier gas and to 3H reconstruction in case of hydrogen carrier gas. The potential barrier in the former surface reconstruction is higher than that in the latter ones. This suggests that carbon incorporation under nitrogen carrier gas is lower than that under hydrogen carrier gas. This theoretical finding is in good agreement with experimental results [51]. More details about impurity and/or dopant incorporation into thin films will be discussed elsewhere [52].

Predictions about the boundaries of these areas on the phase diagram are still semiquantitative. It is due to the difficulty in simultaneously correctly determining the enthalpy of formation of GaN and NH_3 based on the GGA approximation. Therefore, we recommend further improvements by calculating the total energy of systems in hybrid approximations and including the thermal properties of surface determined in our phononic calculations. Accuracy can also be improved using a kinetic-thermodynamic or nonequilibrium model; for example, using steepest-entropy-ascent quantum thermodynamics [53–55].

IV. CONCLUSION

In conclusion, this paper presents systematic improvements in atomistic thermodynamics for III-nitride surfaces by including first-principles phonon calculations. This method allows us to better describe the state of hot surfaces existing during growth by epitaxial methods. We determined vibrational contributions to the free energies for the selected reconstructed polar GaN(0001) surfaces. The results confirm that there are significant discrepancies in the temperature dependencies between some surfaces, especially in the presence of molecules and radicals that retain their molecular nature. We also presented a simple parametrization of thermal dependence of the surface free energy which can be included in the thermodynamic models to more accurately determine the surface state. Using this data, we prepared an improved surface phase diagram of GaN(0001) for the conditions corresponding to the low-pressure MOCVD growth process.

ACKNOWLEDGMENTS

This work was supported in part by the National Science Centre of Poland (Grant No. 2017/27/B/ST3/01899), the MEXT GaN R&D Project and the Collaborative Research Program of the Research Institute for Applied Mechanics, Kyushu University (Project No. 18RE-4). The DFT calculations were carried out with the support of the Interdisciplinary Centre for Mathematical and Computational Modelling at the University of Warsaw (ICM UW) (Grant No. GB76-25).

[1] T. Kachi, Jpn. J. Appl. Phys. **53**, 100210 (2014).
[2] Y. Zhang, A. Dadgar, and T. Palacios, J. Phys. D: Appl. Phys. **51**, 273001 (2018).
[3] H. Amano, Y. Baines, E. Beam, M. Borga, T. Bouchet, P. R. Chalker, M. Charles, K. J. Chen, N. Chowdhury *et al.*, J. Phys. D: Appl. Phys. **51**, 163001 (2018).
[4] P. Kempisty, Y. Kangawa, A. Kusaba, K. Shiraishi, S. Krukowski, M. Bockowski, K. Kakimoto, and H. Amano, Appl. Phys. Lett. **111**, 141602 (2017).
[5] Y. Kangawa, T. Ito, A. Taguchi, K. Shiraishi, and T. Ohachi, Surf. Sci. **493**, 178 (2001).
[6] Y. Kangawa, Y. Matsuo, T. Akiyama, T. Ito, K. Shiraishi, and K. Kakimoto, J. Cryst. Growth **300**, 62 (2007).
[7] T. Ito, T. Nakamura, T. Akiyama, and K. Nakamura, Appl. Surf. Sci. **254**, 7659 (2008).
[8] T. Akiyama, T. Yamashita, K. Nakamura, and T. Ito, J. Cryst. Growth **318**, 79 (2011).
[9] Y. Kangawa, T. Akiyama, T. Ito, K. Shiraishi, and T. Nakayama, Materials **6**, 3309 (2013).
[10] Y. Kangawa, T. Ito, A. Koukitu, and K. Kakimoto, Jpn. J. Appl. Phys. **53**, 100202 (2014).
[11] C. G. Van de Walle and J. Neugebauer, Phys. Rev. Lett. **88**, 066103 (2002).
[12] C. G. Van de Walle and J. Neugebauer, J. Cryst. Growth **248**, 8 (2003).
[13] T. Akiyama, H. Nakane, K. Nakamura, and T. Ito, Phys. Rev. B **94**, 115302 (2016).
[14] A. Kusaba, Y. Kangawa, P. Kempisty, K. Shiraishi, K. Kakimoto, and A. Koukitu, Appl. Phys. Express **9**, 125601 (2016).
[15] L. C. Grabow, J. J. Uhlrich, T. F. Kuech, and M. Mavrikakis, Surf. Sci. **603**, 387 (2009).
[16] L. Lymperakis, J. Neugebauer, M. Himmerlich, S. Krischok, M. Rink, J. Kröger, and V. M. Polyakov, Phys. Rev. B **95**, 195314 (2017).
[17] P. Kempisty, P. Strak, K. Sakowski, Y. Kangawa, and S. Krukowski, Phys. Chem. Chem. Phys. **19**, 29676 (2017).
[18] P. Strak, K. Sakowski, P. Kempisty, I. Grzegory, and S. Krukowski, J. Phys. Chem. C **122**, 20301 (2018).
[19] P. Ordejón, E. Artacho, and J. M. Soler, Phys. Rev. B **53**, R10441 (1996).
[20] J. M. Soler, E. Artacho, J. D. Gale, A. Garcia, J. Junquera, P. Ordejón, and D. Sánchez-Portal, J. Phys.: Condens. Matter **14**, 2745 (2002).
[21] SIESTA, http://departments.icmab.es/leem/siesta.
[22] L. S. Pedroza, A. J. R. da Silva, and K. Capelle, Phys. Rev. B **79**, 201106(R) (2009).
[23] M. M. Odashima, K. Capelle, and S. B. Trickey, J. Chem. Theory Comput. **5**, 798 (2009).
[24] M. Leszczynski, H. Teisseyre, T. Suski, I. Grzegory, M. Bockowski, J. Jun, S. Porowski, K. Pakula, J. M. Baranowski, C. T. Foxon *et al.*, Appl. Phys. Lett. **69**, 73 (1996).
[25] A. Kokalj, Comp. Mat. Sci. **28**, 155 (2003), code available from http://www.xcrysden.org.
[26] K. Shiraishi, J. Phys. Soc. Jpn. **59**, 3455 (1990).
[27] L. Bengtsson, Phys. Rev. B **59**, 12301 (1999).
[28] G. Kresse, J. Furthmuller, and J. Hafner, Europhys. Lett. **32**, 729 (1995).
[29] K. Parlinski and Y. Kawazoe, Phys. Rev. B **60**, 15511 (1999).
[30] A. Togo and I. Tanaka, Scripta Mater. **108**, 1 (2015).
[31] S. Sanna, C. Thierfelder, S. Wippermann, T. P. Sinha, and W. G. Schmidt, Phys. Rev. B **83**, 054112 (2011).
[32] M. Friedrich, A. Schindlmayr, W. G. Schmidt, and S. Sanna, Phys. Status Solidi B **253**, 683 (2016).
[33] D. A. McQuarrie, *Statistical Mechanics* (Harper & Row, New York, 1976).
[34] G.-X. Qian, R. M. Martin, and D. J. Chadi, Phys. Rev. B **38**, 7649 (1988).
[35] Physical constants of organic compounds, in *CRC Handbook of Chemistry and Physics*, 73rd ed., edited by D. L. Lide (CRC Press, Boca Raton, FL, 1972), pp. 5–18.
[36] The NIST Chemistry WebBook, https://webbook.nist.gov.
[37] A. J. Jackson and A. Walsh, Phys. Rev. B **88**, 165201 (2013).
[38] M. Bockowski, M. Iwinska, M. Amilusik, M. Fijalkowski, B. Lucznik, and T. Sochacki, Semicond. Sci. Technol. **31**, 093002 (2016).
[39] Z. Qin, G. Qin, X. Zuo, Z. Xiong, and M. Hu, Nanoscale **9**, 4295 (2017).
[40] J. M. Zhang, T. Ruf, M. Cardona, O. Ambacher, M. Stutzmann, J.-M. Wagner, and F. Bechstedt, Phys. Rev. B **56**, 14399 (1997).

[41] T. Ruf, J. Serrano, M. Cardona, P. Pavone, M. Pabst, M. Krisch, M. D'Astuto, T. Suski, I. Grzegory, and M. Leszczynski, Phys. Rev. Lett. **86**, 906 (2001).

[42] K. Esfarjani and H. T. Stokes, Phys. Rev. B **77**, 144112 (2008).

[43] V. Bermudez, Surf. Sci. Rep. **72**, 147 (2017).

[44] P. Kempisty, P. Strak, and S. Krukowski, Surf. Sci. **605**, 695 (2011).

[45] K. Sekiguchi, H. Shirakawa, K. Chokawa, M. Araidai, Y. Kangawa, K. Kakimoto, and K. Shiraishi, Jpn. J. Appl. Phys. **57**, 04FJ03 (2018).

[46] R. Czernecki, E. Grzanka, R. Jakiela, S. Grzanka, C. Skierbiszewski, H. Turski, P. Perlin, T. Suski, K. Donimirski, and M. Leszczynski, J. Alloys Compd. **747**, 354 (2018).

[47] A. Koukitu and Y. Kumagai, J. Phys.: Condens. Matter **13**, 6907 (2001).

[48] S. Mita, R. Collazo, A. Rice, R. F. Dalmau, and Z. Sitar, J. Appl. Phys. **104**, 013521 (2008).

[49] P. Reddy, S. Washiyama, F. Kaess, R. Kirste, S. Mita, R. Collazo, and Z. Sitar, J. Appl. Phys. **122**, 245702 (2017).

[50] C. B. Alcock, V. P. Itkin, and M. K. Horrigan, Can. Metall. Q. **23**, 309 (1984).

[51] F. Kaess, S. Mita, J. Xie, P. Reddy, A. Klump, L. H. Hernandez-Balderrama, S. Washiyama, A. Franke, R. Kirste, A. Hoffmann *et al.*, J. Appl. Phys. **120**, 105701 (2016).

[52] Y. Kangawa, A. Kusaba, P. Kempisty, K. Shiraishi, S. Nitta, and H. Amano, Appl. Phys. Rev. (to be published).

[53] Y. Inatomi, Y. Kangawa, A. Pimpinelli, and T. L. Einstein, Phys. Rev. Mater. **3**, 013401 (2019).

[54] A. Kusaba, G. Li, M. R. von Spakovsky, Y. Kangawa, and K. Kakimoto, Materials **10**, 948 (2017).

[55] A. Kusaba, G. Li, P. Kempisty, M. R. von Spakovsky, and Y. Kangawa, Materials **12**, 972 (2019).